Materials Today Communications 39 (2024) 108579

Contents lists available at ScienceDirect

Materials Today Communications

journal homepage: www.elsevier.com/locate/mtcomm

Spatial 3D correlation of flux pinning with porosity distribution in $YBa_2Cu_3O_{7-\delta}$ using tensorial neutron tomography

U.K. Oji [a,b,*], A. Hilger [b], I. Manke [b], C. Foerster [b], R. Cubitt [a], N. Kardjilov [b]

[a] Institut Laue-Langevin, Large Scale Structures Group, 71 avenue des Martyrs CS 20156, 38042, Grenoble Cedex 9, France
[b] Helmholtz-Zentrum Berlin für Materialien und Energie (HZB), Berlin D-14109, Germany

ARTICLE INFO

Keywords:
Superconductivity
Polarized neutron imaging
Magnetic structures

ABSTRACT

Engineering devices from High Temperature Superconductors (HTS) for practical applications such as in transport and medical imaging requires an understanding of their critical current density (J_C) distribution and how the material properties affect this. J_C describes the maximum gradient of flux that can be found in a superconductor sustained by vortex pinning which is the preferential positioning of vortex in defective regions of weaker superconductivity. Local correlation of imperfections with high pinning has required destructive methods such as slicing then scanning with local magnetic probes. We describe the first case of non-destructive spatial correlation of flux pinning and consequently J_C with bulk imperfections at different temperatures in top-seeded melt grown (TSMG) $YBa_2Cu_3O_{7-\delta}$ chosen for its high pinning in addition to a rich structure of pores, twins and grain boundaries. This is facilitated by a combination of polarized neutron tomography to image trapped magnetic fields in a range around the material critical temperature and conventional neutron tomography to characterize potential pinning objects. The results indicate that there is indeed preferential trapping in the porous regions independent of the resolvable pore size. Polarized optical microscopy data suggests that the observed phenomenon is attributable to twin boundaries and crack defects located at the pore interface.

1. Introduction

High Temperature Superconductors (HTS) have applications in multiple domains such as in medical imaging, transport and magnetic levitation [1–5]. These all require a capability to transport large currents in the superconducting state. Being type II superconductors, magnetic fields can exist in the bulk of HTS as lines of quantized flux, sustained by a vortex of super-current. Above an applied current that exceeds J_C, these vortices are free to move, creating voltage and hence rendering the superconductor largely useless regarding known applications. A superconductor cooled in an applied field which is subsequently dropped to zero has peak values of trapped field (clusters of vortices) in regions with a high concentration of pinning centres surrounded by the highest field gradients [6,7]. J_C can also be thought of as being proportional to the maximum gradients of these trapped magnetic flux. Engineering imperfections in superconductors to maximize pinning and hence J_C without suppressing the critical temperature or compromising the upper critical field is not a simple task. Being able to spatially correlate potential pinning centres, such as pores, with areas of trapped flux gives highly desirable information for the manufacturers of superconductors based devices.

Several techniques are currently used for the characterization of the pinning distribution and the J_C of superconductors, each with unique limitations. Magnetometry and current-voltage measurements are simple techniques to access the average critical current and the transition temperature (T_C) of a superconductor, but they lack spatial resolution. Magneto-Optical Kerr Effect [8] and local Hall probes [9,10] instead can be used to map the trapped vortex lines after field trapping and establish a correlation with the surface morphology. However these techniques are surface sensitive and the correlation can be done only over the first nanometers below the surface.

Cribier *et al.* [11] have demonstrated that neutron scattering experiments can be utilized to probe magnetic flux structures in superconductors. Indeed, neutrons possess a magnetic moment while being charge neutral, and they thus allow non-destructive characterization of magnetic fields and flux structures in the bulk of materials [12]. More recently, the development of polarized neutron radiography and tomography has shown the neutron's potential to go beyond the limitations of the aforementioned characterization techniques. Flux trapping has been studied in pure Pb superconductors [13] and Tutueanu *et al.*

* Corresponding author at: Institut Laue-Langevin, Large Scale Structures Group, 71 avenue des Martyrs CS 20156, 38042, Grenoble Cedex 9, France.
E-mail address: u.oji@campus.tu-berlin.de (U.K. Oji).

https://doi.org/10.1016/j.mtcomm.2024.108579
Received 7 October 2023; Received in revised form 25 February 2024; Accepted 7 March 2024
Available online 8 March 2024

[14] visualized, in 2D, the dopant concentrations of the cuprate $Lu_{2-x}Sr_xCuO_4$ using polarized neutron radiography. Kardjilov *et al.* [15] showed the potential for 3D visualization through the qualitative tomographic reconstruction of the trapped field in a Pb superconductor. This technique has been further advanced in the work by Hilger *et al.* through the quantitative vectorial reconstruction of the trapped field in a Pb superconductor [16].

Here we show neutron tomography techniques can be used effectively in non-destructive 3D characterization of superconductors. We use a combination of conventional and polarized neutron tomography to explore correlations between the material porosity and field pinning/trapping in a sample of Yttrium Barium Cuprate. This relationship can be used as a proxy to understand the relationship to J_C in superconductors.

2. Materials & methods

2.1. Yttrium barium cuprate

A pseudosingle crystal bulk ingot of $YBa_2Cu_3O_{7-\delta}$ with dimensions of 4 cm× 4 cm× 1 cm was fabricated commercially using standard top-seeded melt growth (TSMG) method. The sample used in the investigation was cut from this and has approximate dimensions of 0.75 cm × 1 cm × 2.5 cm. The sample material shows an inhomogeneous porosity distribution resulting either from the powder compaction before melt processing or from the evolution of oxygen gas during melt processing.

2.2. Magnetometry

DC Magnetometry measurements were performed to determine the transition temperature of the sample via field cooling and increasing the temperature. This was done using an MPMS3 quantum interference device (SQUID) magnetometer. A cut of the sample was made at an arbitrary position from the bulk with dimensions 4 mm × 4 mm× 1 mm and was placed on a quartz rod using a non-static tape. The applied field was the remnant field of the SQUID system which was about 0.07 mT (H||c). The sample was field cooled to 88 K and temperature was swept up to 94 K at a rate of 1 K/min. Fig. 1 shows the normalized magnetization measured as a function of this temperature increase. T_C was determined to be 91.3 K with a ΔT of less than 1 K, defined as difference in temperature between 10% and 90% of the total magnetization signal. YBCO typically has a superconducting transition temperature (T_C) of 91 ± 1 K [17]. Practically, this value can be modified through doping, stresses and inhomogeneities in the sample bulk [18,19]. The sharpness of the transition can be an indication of the purity of the sample based on high quality single crystals of YBCO showing transition widths of less than 1 K [20].

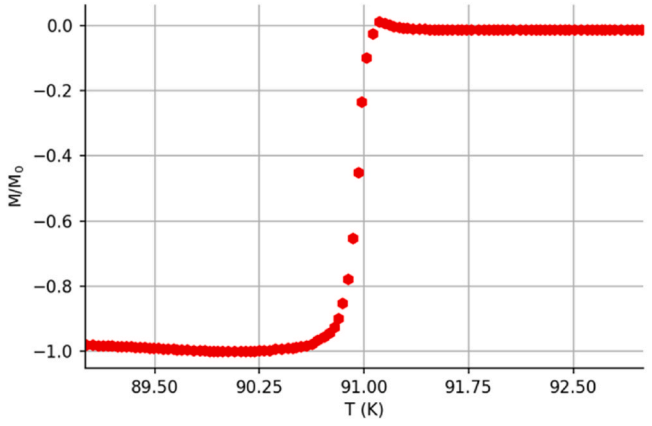

Fig. 1. Normalized magnetization measured as a function of increasing temperature with an applied field of 0.07 mT (H||c). The 4 mm × 4 mm× 1 mm sample of $YBa_2Cu_3O_{7-\delta}$ stops being superconducting at T = 91.3 K.

2.3. Neutron attenuation tomography

The internal morphology of the sample was studied using Neutron Attenuation Tomography performed on the CONRAD-2 imaging station at Helmholtz Zentrum Berlin (HZB). This was measured at room temperature and zero applied magnetic field. The station is situated at the end of a curved neutron guide facing the cold source of the 10 MW BER-II research reactor. The neutron beam is polychromatic with a wavelength range of 2 Å −6 Å and a neutron flux of 3×10^9 n/s/cm^2 at the pinhole. The beam size at the sample position, 5 m away from the pinhole, was approximately 10 cm × 10 cm. The detector system was based on a 16-bit CCD camera with 2048 × 2048 pixels with each pixel having a size of 28 μm. The images obtained from the ^{6}LiF:ZnS 200 μm scintillator were projected via a mirror and a lens system onto the CCD chip. For this work, 500 projections were collected while the sample was rotated around a fixed axis. The rotation interval was 360° with a measuring time per projection of 20 s. A standard back-projection algorithm has been used for the 3D volume reconstruction.

2.4. Polarized neutron tomography

Internal distribution of the trapped field in the sample was investigated using Polarized Neutron Tomography at the imaging station V19, also located at HZB [21]. The instrument operates with spin-polarized neutrons of a wavelength 3.2 Å. The incident neutron beam is spin polarized via a solid state bender that works in transmission resulting in a polarization of 85%. The polarized beam is further collimated by a soller collimator. This polarized beam then interacts with the sample inside a closed-cycle cryostat that allows cooling down to a temperature of 4.0 K. With negligible scattering from the system, the neutron spin interacts with the magnetic field along the neutron's path and the final beam is spin analyzed by a solid state bender that works in reflection before arriving at the detector.

Field trapping in the sample is achieved by cooling to 90.5 K in a magnetic field of 0.5 mT produced by a Helmholtz coil then subsequently switching off this applied field. The field, H_a, was applied in the X direction perpendicular to the neutron beam travel as illustrated in Fig. 2. The low value of 0.5 mT was chosen such that the beam polarization precessed no more than a π rotation. The temperature of the sample was then increased by 0.1 K up to 90.9 K. For each of the steps the full 3 × 3 sets of polarized neutron tomography data (polarization in X,Y,Z and analysis for each X, Y, Z Cartesian directions) are obtained. 51 radiographic projections are involved for each tomography with 120 s exposure time per projection. A reconstruction of the magnetic field distribution in 3D was performed using the tensorial algebraic reconstruction technique (TMART) [16]. The chosen temperature and applied magnetic fields for the experiment are unlikely to be used for practical superconducting applications but it is assumed that correlations between any observed spatial variance of the superconducting properties based on the material morphology are likely to be relevant over a wide range of temperatures and fields. More details related to the experimental technique and to the theory of TMART reconstruction algorithm can be found in the Supplementary Information.

3. Results

Using ImageJ, the reconstructed volume from the attenuation tomography can be further analyzed to give the internal pore distribution. This volume is shown in Fig. 3 in addition to further analysis to determine the distribution volume characteristics. Fig. 3a shows the internal pore distribution from the different perspectives. Fig. 3b focuses on the perspective of the *x-z* plane. The projection of the corresponding normalized attenuation along the *x* axis (averaged over the y & z axes) is used as a proxy to study the density of the material given the proportionality between the material density and attenuation. From this it can be inferred that the maximum porosity value in the sample along x is

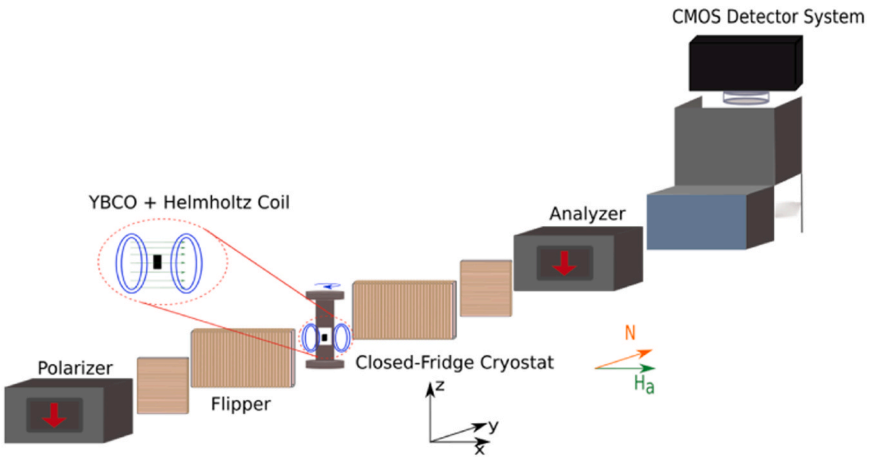

Fig. 2. Schematic of the Polarized Neutron Tomography experiment comprising of the spin polarizers, the closed fridge cryostat, spin flippers and a Complementary metal-oxide-semiconductor (CMOS) detection system.

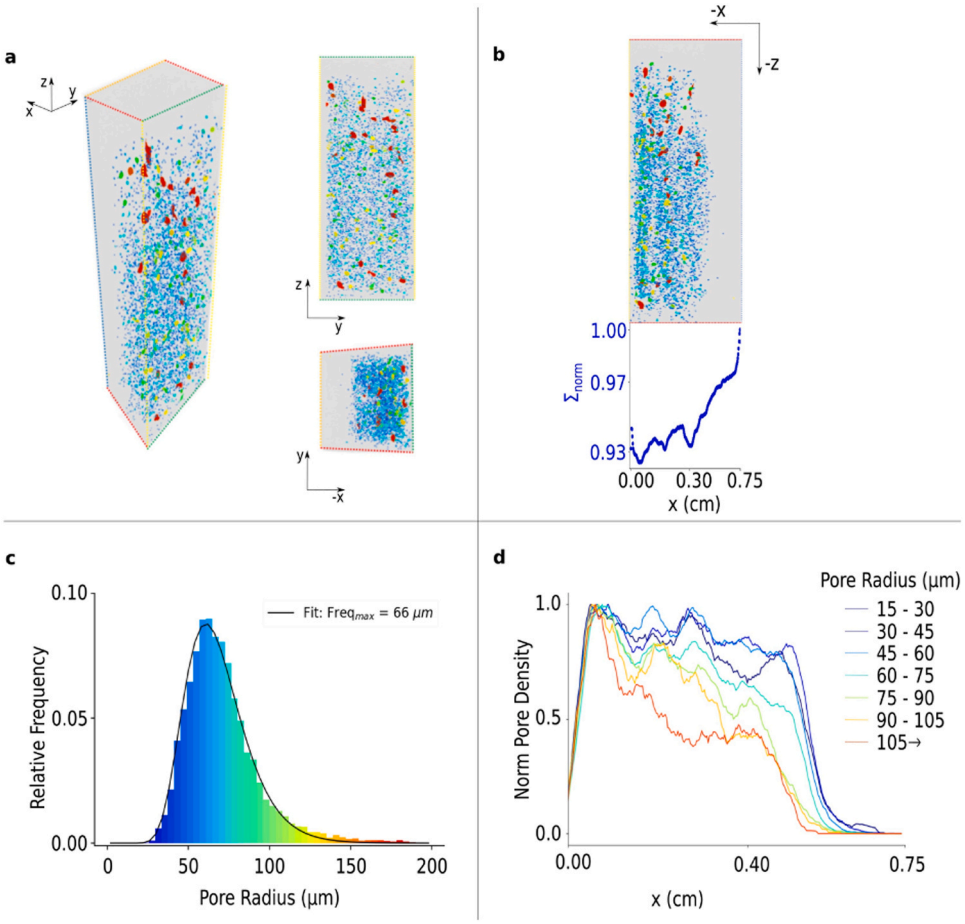

Fig. 3. (a) Visualization of the spatial distribution of pores in the sample with the perspective in different Cartesian planes indicated by the arrows. The pores are coloured based on size and follow the same colour scheme through the entire figure. (b) Visualization of the pore spatial distribution with the perspective along the x-z plane. The projection of the mean neutron attenuation along the x axis (averaged over the y & z axes) is plotted below. This value is proportional to the material density and suggests a maximum sample porosity ~ 7.6%. (c) Pore radius distribution: the radii range between 15 μm and 200 μm with the most abundant pores having a radius of about 66 μm. (d) Normalized mean pore density along the x axis plotted by pore radius. No significant difference in the spatial distribution of pores of different size.

7.6% assuming 100% density of material in the non-porous region. The pore radius distribution, depicted in Fig. 3c, ranges from approximately 15 to 200 µm, with the most prevalent pores having a radius of 66 µm. With 86.5% of the resolvable pores having a radius of more than 50 µm, it can be concluded that they result from evolution of oxygen gas during the melt processing [22]. This does not however exclude the existence of pores in the bulk resulting from the powder compaction as they would likely have sizes unresolvable via the current conventional tomography

setup. From Fig. 3a, there, is no clear spatial dependence of the pore distribution by size. This is confirmed in Fig. 3d where we show the projection of the normalized pore density along the *x* axis for different pore size ranges. There is no significant difference in the forms of the graphs that is unaccountable for by the differences in relative frequency of the pores by size (Fig. 3c)

Fig. 4 shows the reconstructed magnetic vector field in addition to the overlay of the field magnitudes to the pore distribution volume. Fig. 4a shows the magnetic vector field obtained from the reconstructed polarized neutron tomography data. The image is shown from the plan view perspective and depicts the evolution of the trapped magnetic vector field as the temperature is increased. Overlaying the attenuation and polarized tomography results offers further insights into the effects of the observed porosity on the sample superconductivity. This can be seen in Fig. 4b & c. The magnitude of the magnetic field is visualized for clarity.

4. Discussion

A first observation is that the maximum value of trapped field in the reconstruction is 0.74 mT, higher than the applied field value of 0.5 mT. The higher field magnitudes are predominantly in the most porous regions of sample (Fig. 4c). A possible hypothesis is that this is a result of the Meissner effect from field cooling as suggested by Pawel *et al.* [23]. Pores in the material, being regions of non-superconductivity, will have a higher magnetic field density due to expulsion of the field into these areas. A more plausible scenario however is that by cooling below T_C, the magnetic field existing in the pores would be frozen in by circulating super-currents and at the same time the flux lines are attracted to defects at the interface of the pores which act as pinning centres [24,25]. This agrees with the work of Jou *et al.* [26] who visualized preferential flux pinning around pores in YBCO through cobalt decoration. With the pore size much larger than the typical vortex separation of 0.1–1 microns [27], multiple vortices would be drawn to and then pass through each pore. At the surfaces where the vortices enter and exit it is not difficult to imagine a higher field density than that applied. The mean trapped magnetic field value of 0.4 mT in the sample remained lower than the value of the applied magnetic field. In Fig. 4a, we can observe a significant deviation of the trapped field direction with respect to the applied one, which cannot be explained simply by the presence of pores. We hypothesize that this results from the orientation of the grains within the sample; this will be the subject of a future study.

Fig. 5 illustrates the evolution of the trapped field magnitude with temperature and its dependence on the sample porosity. Fig. 5b shows the normalized pore density projected along the x axis (red curve) as seen in Fig. 5a. The projections of the trapped field magnitude on the *x* axis per temperature value (Fig. 5b) make apparent the dependence of trapped field retention on the bulk porosity. After field cooling to 90.5 K and switching off the field, the peak of the mean trapped field is found around the centre of the sample. On subsequent heating, the peak progressively shifts towards the regions with a higher pore density. Furthermore, there appears to be a correlation between the profile of the trapped field on heating with that of the pore density. The preferential field retention in these regions is most likely due to the preferential flux pinning in the defective regions at the pore interfaces. It is known that the pinning potential at the interface of non-superconducting regions of the size in the order of the observed pores is much larger than the that of smaller pinning sites with sizes in the order of the coherence lengths which in YBCO is less than 1.6 nm at low temperatures and 10–30 nm at the relevant temperatures [28–31]. For example the potentials for small

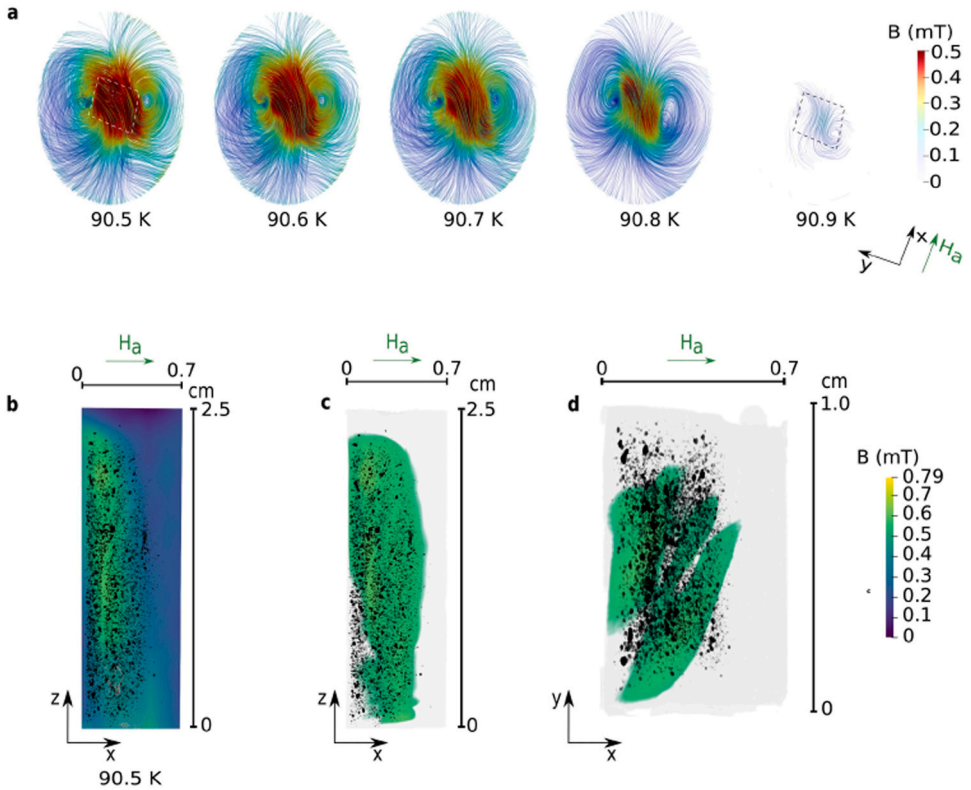

Fig. 4. (a) Plan view streamline visualization of the vector field reconstruction of the trapped field in the sample of $YBa_2Cu_3O_{7-\delta}$ from Polarized Neutron Tomography after field cooling to 90.5 K and switching off the field. The sample temperature is increased in steps of 0.1 K to 90.9 K and the remaining trapped field is reconstructed using the same procedure (Dotted lines show the sample outline). (b) 3D Overlay of the pore distribution with the magnitude of the reconstructed vector field after field cooling and switching off the field at 90.5 K. (c) 3D Overlay of the pore distribution with the magnitude of the trapped field at 90.5 K masking out $B < \mu_0 H_a$ is shown from the *x*-*z* and (d) *x*-*y* perspectives. Regions of $B > \mu_0 H_a$ correspond with regions of high porosity. The volume of *B* in (b), (c) and (d) are transparent.

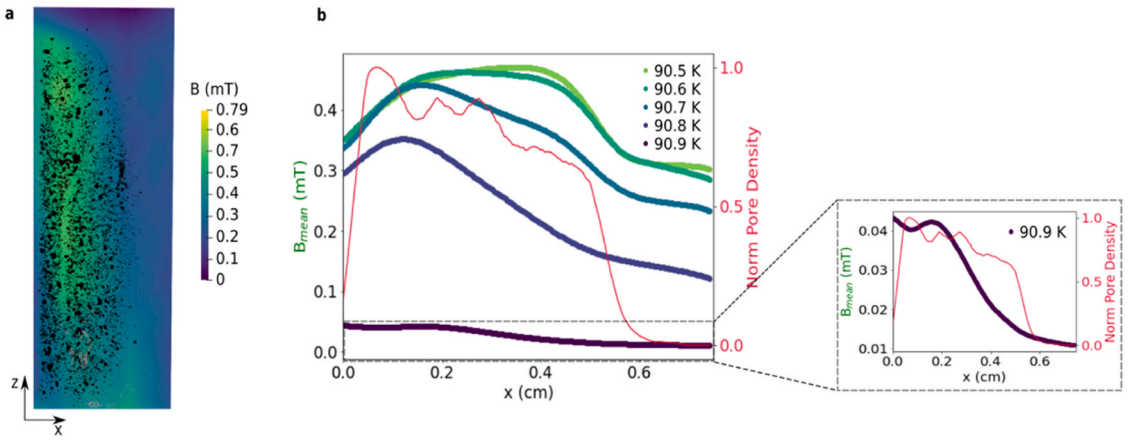

Fig. 5. (a) Overlay of the magnetic field magnitude with the pore distribution from the x-z perspective. (b) Mean field of the sample averaged over the y and z axes (projected along the x axis) at the different experiment temperatures overlayed with the normalized pore density averaged in the same manner. The mean field peaks in a central position at 90.5 K. The peak progressively moves towards the regions of high porosity on heating the sample.

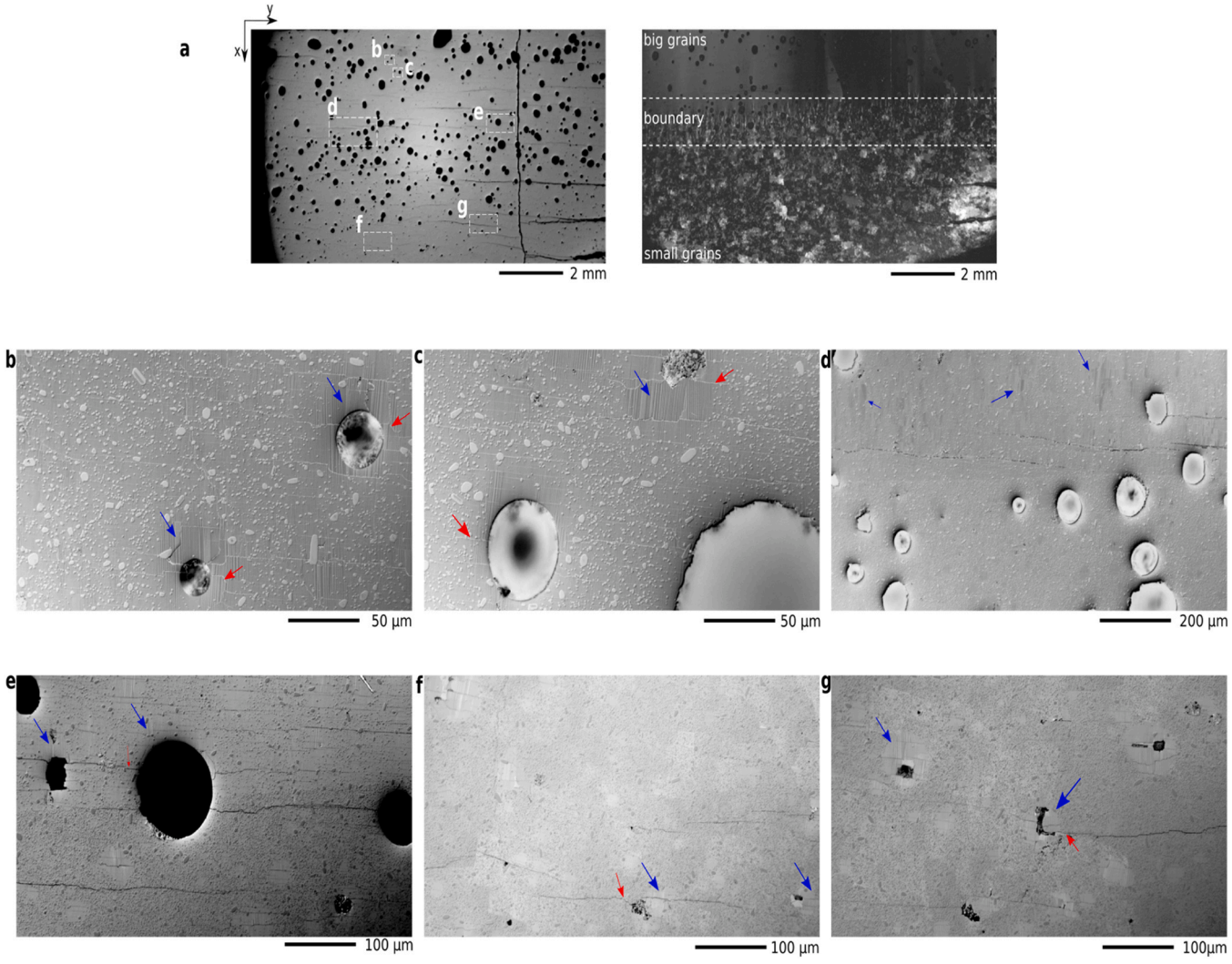

Fig. 6. (a) Microscopy images at sample height displaying notable porosity (left) and Differential Interference Contrast Image (right) illustrating the separation into large grain regions with high porosity and small grain regions with low porosity. Y211 particles are observed with consistent concentration across regions, while cracks (red arrows) are observed throughout. Higher concentration of twin boundaries (blue arrows))in large grain regions (b-c) compared to low grain regions (f-g), with a visible transition at the boundary (d-e). Twin boundaries are also observable at pore interfaces, including those in regions of low porosity.

and large pinning sites are of the form $\frac{H_c^2}{8\pi}\frac{4}{3}\pi\xi^3$ and $\frac{H_c^2}{8\pi}\pi\xi^2 d$ respectively [24,25] where ξ is the superconducting coherence length and d is the size of the site. This means that the interfacial pinning observed in the porous regions are less susceptible to thermal fluctuations and could explain the higher field retention observed. In addition to interfacial pinning, field is likely trapped inside the pores as multiple flux quanta due to the circulating super-currents flowing around the pores in the material bulk [32].

Polarized Optical Microscopy is used to investigate the material structure to elucidate the observed correlation of the field trapping with the pore distribution. The sample is cut and polished at a height with observable porosity. The results of this investigation are shown in Fig. 6. The surface appears to be separated into three regions of interest, the top region associated with the a higher porosity in the sample, the bottom region associated with lower porosity and the boundary region between these two. The top region is composed of significantly larger grains while the bottom regions is made up of smaller grains.

For all the regions, Y211 particles can be observed with no significant difference in their distribution through the surface. The images indicate the sample is rich with defects. Cracks are observed to manifest through the samples. The Y211 particles with a typical size of more than 0.24 μm are known to be at the origin of these cracks [33]. These cracks appear also in the vicinity of the pores which would enhance the flux pinning at these regions. Furthermore, twin boundaries are present through the sample with a higher concentration of them being in the regions of higher porosity. Notably, a prominent correlation emerges between the presence of twin boundaries and pores, with twin boundaries manifesting at the interfaces of the pores, including those within regions of low porosity. The presence of these defects at the pore interfaces would explain the observation of a correlation between the field trapping in the material and the pore distribution from the polarized neutron tomography experiment. Their presence would serve to enhance flux pinning in the pore vicinity in addition to the effects of the Y211 particles.

From Fig. 3d, the spatial distribution of pores does not differ significantly based on their radii. This indicates a more or less isotropic distribution of pores based on radius in the more porous regions and explains the apparent independence of the field retention in the porous regions on pore radius for the resolvable pores. Existence of pinning sites such as the Y211 particles, cracks and twin boundaries have been confirmed using Polarized Optical Microscopy and would play a role in flux trapping in the regions of negligible observable porosity. Pores in the length scale closer to the coherence length of YBCO can not be exempted from the sample too as they would only be too small to be resolved using the current neutron attenuation tomography setup.

5. Conclusion

Using Neutron Tomography as a primary characterization method, we have been able to visualize the effect of material morphology, specifically the porosity on field trapping and retention in YBCO high T_C superconductor. The non-destructive characterization highlights on the flux pinning on the interfaces of such defects and the effects on the thermal susceptibility of the trapped flux. The mechanism for the flux pinning has been elucidated using Polarized Optical Microscopy to show the presence of Y211 particles in the material and defects such as twin boundaries and cracks at the interface of the pores. The interfacial defects in combination with the particles will enhance the flux pinning in the porous regions.

These results highlight the utility of neutron tomography as a primary tool for the non-destructive investigation of superconducting materials for engineering applications. Beyond correlations with porosity, the method of polarized neutron tomography allows the investigation of superconducting properties with properties such as defect concentration, doping concentration and granularity in a bulk superconducting sample. Furthermore, the reconstructed vector field of the trapped field in the superconductor can facilitate the non-destructive determination of the critical current distribution in the bulk. That is beyond the scope of this paper and will be the subject of a future study.

Declaration of Competing Interest

The authors declare that they have no known competing financial interests or personal relationships that could have appeared to influence the work reported in this paper.

Data availability

Data will be made available on request.

Acknowledgements

The neutron tomography experiments were performed at the Helmholtz Zentrum Berlin. This work was jointly funded by Institut Laue Langevin and the Helmholtz Zentrum Berlin. We thank the Neel Institute Magnetometry Platform (PMag) for access to the magnetometry facilities. The authors wish to acknowledge the technical contributions of M. Krzyzagorski and M. Osenberg from the Helmholtz Zentrum Berlin.

Appendix A. Supporting information

Supplementary data associated with this article can be found in the online version at doi:10.1016/j.mtcomm.2024.108579.

References

[1] M. Tomita, M. Murakami, High-temperature superconductor bulk magnets that can trap magnetic fields of over 17 tesla at 29 K, Nature 421 (6922) (2003) 517–520, https://doi.org/10.1038/nature01350.
[2] A. Patel, A. Baskys, T. Mitchell-Williams, A. McCaul, W. Coniglio, J. Hänisch, M. Lao, B.A. Glowacki, A trapped field of 17.7 T in a stack of high temperature superconducting tape, Supercond. Sci. Technol. 31 (9) (2018) 09LT01, https://doi.org/10.1088/1361-6668/aad34c.
[3] J. Jiang, Y. Zhao, Y. Li, L. Zhao, Y. Zhang, Trapped field and levitation performance of a YBCO superconductor magnetized in different external magnetic fields, J. Supercond. Nov. Magn. 32 (7) (2019) 1885–1890, https://doi.org/10.1007/s10948-018-4912-4.
[4] G. Fuchs, P. Schätzle, G. Krabbes, S. Gruß, P. Verges, K.-H. Müller, J. Fink, L. Schultz, Trapped magnetic fields larger than 14 T in bulk $YBa_2Cu_3O_{7-x}$, Appl. Phys. Lett. 76 (15) (2000) 2107–2109, https://doi.org/10.1063/1.126278.
[5] T.M. Silver, S.X. Dou, J.X. Jin, Applications of high temperature superconductors, Eur. News 32 (3) (2001) 82–86, https://doi.org/10.1051/epn:2001302.
[6] M. Murakami, Melt processed high-temperature superconductors (Ed.), World Scientific, Singapore, 1992.
[7] D.A. Cardwell, Processing and properties of large grain (RE)BCO, Mater. Sci. Eng. B 53 (1-2) (1998) 1–10, https://doi.org/10.1016/S0921-5107(97)00293-6.
[8] A.A. Polyanskii, A. Gurevich, J. Jiang, D.C. Larbalestier, S.L. Bud'ko, D. K. Finnemore, G. Lapertot, P.C. Canfield, Magneto-optical studies of the uniform critical state in bulk MgB_2, Supercond. Sci. Technol. 14 (10) (2001) 811–815, https://doi.org/10.1088/0953-2048/14/10/301.
[9] M. Carrera, J. Amor, S.X. Obradors, J. Fontcuberta, A new method of computation of current distribution maps in bulk high-temperature superconductors: analysis and validation, Supercond. Sci. Technol. 16 (10) (2003) 1187–1194, https://doi.org/10.1088/0953-2048/16/10/311.
[10] M. Carrera, X. Granados, J. Amoroś, R. Maynou, T. Puig, X. Obradors, Computation of critical current in artificially structurated bulk samples from Hall measurements, J. Phys.: Conf. Ser. 97 (2008) 012107, https://doi.org/10.1088/1742-6596/97/1/012107.
[11] D. Cribier, B. Jacrot, L. Mahdav Rao, B. Farnoux, Study of the superconductive mixed state by neutron diffraction, Prog. Low. Temp. Phys. 5 (1967) 20, https://doi.org/10.1016/S0079-6417(0)60122-5.
[12] M. Strobl, H. Heimonen, S. Schmidt, M. Sales, N. Kardjilov, A. Hilger, I. Manke, T. Shinohara, J. Valsecchi, Polarization measurements in neutron imaging, J. Phys. D: Appl. Phys. 52 (12) (2019) 123001, https://doi.org/10.1088/1361-6463/aafa5e.
[13] W. Treimer, O. Ebrahimi, N. Karakas, R. Prozorov, Polarized neutron imaging and three-dimensional calculation of magnetic flux trapping in bulk of superconductors, Phys. Rev. B 85 (18) (2012) 184522, https://doi.org/10.1103/PhysRevB.85.184522.
[14] A.E. Ţuţueanu, M. Sales, K. Eliasen, M.E. Lăcătus¸u, J.-C. Grivel, N. Kardjilov, I. Manke, M. Krzyzagorski, Y. Sassa, M. Andersson, S. Schmidt, K. Lefmann, Non-destructive characterisation of dopant spatial distribution in cuprate

superconductors, Phys. C 575 (2020) 1353691, https://doi.org/10.1016/j.physc.2020.1353691.
[15] N. Kardjilov, I. Manke, M. Strobl, A. Hilger, W. Treimer, M. Meissner, T. Krist, J. Banhart, Three-dimensional imaging of magnetic fields with polarized neutrons, Nat. Phys. 4 (5) (2008) 399–403, https://doi.org/10.1038/nphys912.
[16] A. Hilger, I. Manke, N. Kardjilov, M. Osenberg, H. Markötter, J. Banhart, Tensorial neutron tomography of three-dimensional magnetic vector fields in bulk materials, Nat. Commun. 9 (1) (2018) 4023, https://doi.org/10.1038/s41467-018-06593-4.
[17] I. Kotsis, M. Enisz, T. Korim, Hot pressing of YBCO-type superconductors, Superlattice Microst. 21 (3) (1997) 435–446, https://doi.org/10.1006/spmi.1996.0414.
[18] S. Dadras, S. Falahati, S. Dehghani, Effects of graphene oxide doping on the structural and superconducting properties of $YBa_2Cu_3O_{7-\delta}$, Phys. C 548 (2018) 65–67, https://doi.org/10.1016/j.physc.2018.02.010.
[19] X.J. Chen, H.Q. Lin, C.D. Gong, Pressure dependence of Tc in Y-Ba-Cu-O superconductors, Phys. Rev. Lett. 85 (10) (2000) 2180–2183, https://doi.org/10.1103/PhysRevLett.85.2180.
[20] R. Liang, D. Bonn, W. Hardy, Growth of high quality YBCO single crystals using BaZrO3 crucibles, Phys. C 304 (1-2) (1998) 105–111, https://doi.org/10.1016/S0921-4534(98)00275-5.
[21] W. Treimer, O. Ebrahimi, N. Karakas, S. Seidel, PONTO—An instrument for imaging with polarized neutrons, Nucl. Instrum. Methods A 651 (1) (2011) 53–56, https://doi.org/10.1016/j.nima.2011.01.009.
[22] D.K. Namburi, Y. Shi, D.A. Cardwell, The processing and properties of bilk (RE) BCO high temperature superconductors: current status and future perspectives, Supercond. Sci. Technol. (Jan. 2021), https://doi.org/10.1088/1361-6668/abde88.
[23] P. Fiertek, B. Andrzejewski, W. Sadowski, Synthesis and transport properties of porous superconducting ceramics of $YBa_2Cu_3O_{7-\delta}$, Rev. Adv. Mater. Sci. 23 (2010) 6.
[24] M. Murakami, H. Fujimoto, S. Gotoh, K. Yamaguchi, N. Koshizuka, S. Tanaka, Flux pinning due to nonsuperconducting particles in melt processed YBaCuO superconductors, Phys. C 185–189 (1991) 321–326, https://doi.org/10.1016/0921-4534(91)91993-E.
[25] M. Murakami, S. Gotoh, H. Fujimoto, K. Yamaguchi, N. Koshizuka, S. Tanaka, Flux pinning and critical currents in melt processed YBaCuO superconductors, Supercond. Sci. Technol. 4 (1S) (1991) S43–S50, https://doi.org/10.1088/0953-2048/4/1S/005.
[26] C.J. Jou, E.R. Weber, J. Washburn, W.A. Soffa, Decoration of flux pinning positions in $YBa_2Cu_3O_{7-\delta}$ superconductors, Appl. Phys. Lett. 52 (4) (1988) 326–327, https://doi.org/10.1063/1.99650.
[27] S.L. Lee, P.G. Kealey, E.M. Forgan, S.H. Lloyd, T.M. Riseman, D.M. Paul, S. T. Johnson, C. Simon, C. Goupil, A. Pautrat, R. Cubitt, P. Schleger, C. Dewhurst, C. M. Aegerter, C. Ager, Small-angle scattering from the vortex lattice in high-[1] and other superconductors, Phys. B (2000), https://doi.org/10.1016/S0921-4526(99)01680-4.
[28] G. Deutscher, K.A. Müller, Origin of superconductive glassy state and extrinsic critical currents in high- Tc oxides, Phys. Rev. Lett. 59 (15) (1987) 1745–1747, https://doi.org/10.1103/PhysRevLett.59.1745.
[29] T.K. Worthington, W.J. Gallagher, T.R. Dinger, Anisotropic nature of high-temperature superconductivity in single-crystal $YBa_2Cu_3O_{7-x}$, Phys. Rev. Lett. 59 (10) (1987) 1160–1163, https://doi.org/10.1103/PhysRevLett.59.1160.
[30] K. Winzer, G. Kumm, Fluctuation-enhanced conductivity and magnetoconductivity of high-quality YBa_2Cu_3O crystals, Z. Phys. B Con Mat. 82 (1991) 5, https://doi.org/10.1007/bf01357171.
[31] A. Hassan, A. Labrag, A. Taoufik, M. Bghour, H. Quaddi, A. Tirbiyine, B. Lmouden, A. Hafid, H. Hamidi, Magnetic penetration depth and coherence length in single-crystal $YBa_2Cu_3O_{7-\delta}$, Phys. Status Solidi B (2021) 2100292, https://doi.org/10.1002/pssb.202100292.
[32] J. Babiskin, Magnetic properties of a hollow superconducting lead sphere, Phys. Rev. 85 (1) (1952) 104–106, https://doi.org/10.1103/PhysRev.85.104.
[33] D. Pavel Cracking, in melt-processed RE-Ba-Cu-O, Supercond. Sci. Technol. 11 (1) (1998) 6–72, https://doi.org/10.1088/0953-2048/11/1/014.